Differential Reynolds stress model and grid adaptation for hypersonic double wedge simulations

A. Bosco[1], B. Reinartz[2] and S. Müller[3]

[1]*Aachen Institute for Advanced Study in Computational Engineering Science, RWTH Aachen, Schinkelstrasse 2, 52062 Aachen, Germany, bosco@aices.rwth-aachen.de*

[2]*Chair for Computational Analysis of Technical Systems, RWTH Aachen, Schinkelstrasse 2, 52062 Aachen, Germany reinartz@cats.rwth-aachen.de*

[3]*Institut für Geometrie und Praktische Mathematik, RWTH Aachen, Templergraben 55, 52056 Aachen , Germany, mueller@igpm.rwth-aachen.de*

Abstract — The simulation of hypersonic flows presents some difficulties due to the interaction between boundary layer and shock waves and its 3D character. In order to achieve more accurate numerical results with respect to physics, a Reynolds stress model (RSM) has been implemented in the well validated Reynolds averaged Navier-Stokes solver QUADFLOW. The RSM developed and tested by Eisfeld, showed promising results on structured grids and is now ready to be used in combination with grid adaptation for solving highly applied complex 3D flows.

1. Introduction

The aerodynamic design of hypersonic inlets is a critical issue for the overall performance of an air breathing propulsion system. Two phenomena characterize the technological problems of the inlet: on the one hand, the interaction of strong shock waves with thick hypersonic boundary layers causes large separation zones that reduce the captured mass flow and thus the engine performance. On the other hand, the high total enthalpy of the flow leads to severe aerodynamic heating, further enhanced by turbulent heat fluxes.

Currently, most of the turbulent flows are studied through the mean of the Reynolds Averaged Navier-Stokes (RANS) method, where the averaged governing equations are solved for the mean variables. For what concerns the turbulent closure, eddy viscosity models are widely employed since they are easy to implement and computationally convenient. Nevertheless these models show difficulties to correctly predict flow phenomena like shock boundary-layer interaction, which are of great interest for hypersonic flow.

For this reason, a differential Reynolds stress model, the SSG/LRR-ω model [1], has been implemented into QUADFLOW [2]. This solver is a parallel adaptive compressible flow solver which employs locally refined meshes with hanging nodes [3].

2. QUADFLOW Solver

QUADFLOW solves RANS equations around complex aerodynamical configurations using a variety of turbulence models. It uses a cell-centered finite volume method on locally adaptive grids. For the computation of the convective flux the AUSMDV Riemann solver is employed [4]. A great advantage of this scheme is the reduction of numerical viscosity.

For what concerns the computation of the viscous fluxes, the gradients of the variables at cell interfaces are determined using the divergence theorem. The computations presented here are
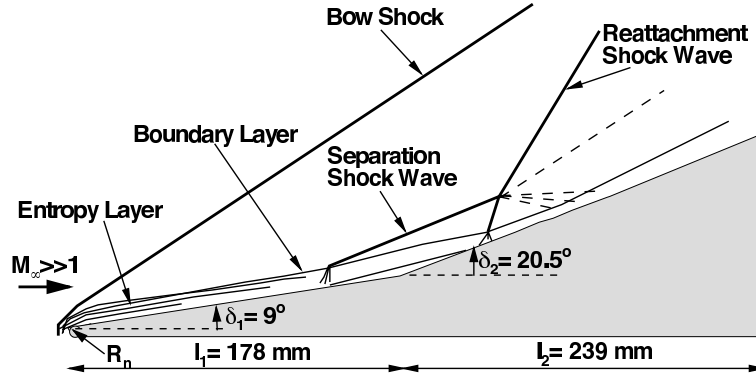
Figure 1: Shock / boundary layer interaction on a hypersonic inlet [5].

steady state analyses so that time plays the role of an iteration parameter to achieve asymptotically stationary flow in the computation. The numerical methods employed are a Runge-Kutta fifth-order explicit scheme and a Backward Euler time integration for implicit treatment. In the QUADFLOW solver, different turbulent models can be chosen. These are all RANS eddy viscosity models, in which the same proportionality between Reynolds stress tensor and the strain rate tensor as for the viscous stresses of a Newtonian fluid in laminar flow is considered. Even though these models are easy to implement and computationally convenient, they appear to be not suitable to simulate flow phenomena like shock boundary layer interaction in hypersonic flow.

2.1. Adaptive technique

The mesh adaptation is performed by means of multiscale techniques similar to those used in data compression. Starting point of this strategy is a sequence of nested grids $G_l := \{\Omega_{li}\}_{i \in I_l}$ that can be obtained by successfully refining the cells on a given coarsest scale $l = 0$ i.e each cell on a coarse scale l is the union of cells on the finer scale $l + 1$. The index set I_l represents the enumeration of the cells corresponding to the grid G_l and corresponding averages $\bar{\mathbf{u}}_l$. By means of this sequence, the average $\bar{\mathbf{u}}_L$ on the finest level L is successively decomposed into a sequence of averages on the coarsest level $\bar{\mathbf{u}}_0$ and details $\bar{\mathbf{d}}_l$, $l = 0, ..., L - 1$; this is realized by a multiscale analysis using biorthogonal wavelets [3].

The detail coefficients can be interpreted as differences between successive refinement levels, which become negligibly small in regions where the solution is sufficiently smooth. The set of significant details can now be introduced $D_\epsilon := \{(l, i) : |d_{l,i}| > \epsilon_l\}$ where $\epsilon_l = 2^{l-L}\epsilon$ is a level-dependent threshold value and the parameter ϵ which determines the sensitivity of the adaptation is user defined. At this point one has to determine the adaptive grid on the new time level. Since the corresponding averages, respectively details are not yet available, one has to predict all details on the new time level that can become significant due to the evolution by means of the details on the old time level. In order to do that an heuristic approach taking into account the finite speed of propagation and the fact that gradients may become steeper causing significant details in the local neighborhood and on higher refinement levels respectively. By means of D_ϵ a locally refined grid with hanging nodes is determined by proceeding from coarse to fine. If there exists a significant detail the corresponding cell is refined. For the flow fields

considered, the number of significant detail coefficients $N_D := \#D_\epsilon$, is much smaller than the number of averages N_L corresponding to the uniform finest scale, i.e. the computational time and memory requirements are significantly reduced.

3. Reynolds Stress Transport Equations

The more accurate level of RANS turbulence models are the differential Reynolds Stress Models where an equation is written and solved for each component of the symmetric Reynolds tensor. The Reynolds stress transport equations for the Reynolds stresses R_{ij}, read as follows:

$$\frac{\partial}{\partial t}(\bar{\rho}\tilde{R}_{ij}) + \frac{\partial}{\partial x_k}(\bar{\rho}\tilde{U}_k\tilde{R}_{ij}) = \bar{\rho}P_{ij} + \bar{\rho}\Pi_{ij} - \bar{\rho}\epsilon_{ij} + \bar{\rho}D_{ij} + \bar{\rho}M_{ij} \quad . \tag{1}$$

where the symbols (¯) and (˜) represent the simple average and the Favre average respectively. The terms that appear at the right hand side of the equation represent the production, the redistribution, the destruction, the diffusion and the contribution of the turbulent mass flux, respectively. The production term

$$\bar{\rho}P_{ij} = -\bar{\rho}\tilde{R}_{ik}\frac{\partial \tilde{U}_j}{\partial x_k} - \bar{\rho}\tilde{R}_{jk}\frac{\partial \tilde{U}_i}{\partial x_k} \tag{2}$$

does not need modeling because it only depends on quantities for which an equation is solved. The other terms need to be modeled and the way the terms are modeled determines the particular type of Reynolds Stress Model.

3.1. The SSG/LRR-ω model

The model chosen to be implemented in QUADFLOW is the SSG/LRR-ω [1]. This model has been developed by Eisfeld and is the combination of the SSG model [7] in the far field and the LRR model near the wall [6]. The idea is to extend the applicability of the SSG model to wall-bounded flows in conjunction with an ω-equation. The LRR model chosen is a simplified version by Wilcox who coupled it with his ω-equation [8]. The choice of this model near the wall is justified by the desire of having a low-Reynolds model allowing integration up to the wall. As Wilcox shows, the near-wall behavior of second-order closure models is strongly influenced by the scale-determining equation [8]. Models based on an ω-equation often predict acceptable value of the wall integration constant and are quite easy to integrate through the viscous sublayer with respect to models based on the ϵ-equations. The omega equation of Menter [9] has been chosen to provide a turbulent length scale for the present model. The blending function of Menter has been employed to smoothly blend the coefficients of the two models.

The re-distribution term is modeled as follows

$$\bar{\rho}\Pi_{ij} = -(C_1\bar{\rho}\epsilon + \frac{1}{2}C_1^*\bar{\rho}P_{kk})\tilde{b}_{ij} + C_2\bar{\rho}\epsilon(\tilde{b}_{ik}\tilde{b}_{kj} - \frac{1}{3}\tilde{b}_{mn}\tilde{b}_{mn}\delta_{ij}) \tag{3}$$

$$+(C_3 - C_3^*\sqrt{II})\bar{\rho}\tilde{k}\tilde{S}_{ij}^* + C_4\bar{\rho}\tilde{k}(\tilde{b}_{ik}\tilde{S}_{jk} + \tilde{b}_{jk}\tilde{S}_{ik} - \frac{2}{3}\tilde{b}_{mn}\tilde{S}_{mn}\delta_{ij}) + C_5\bar{\rho}\tilde{k}(\tilde{b}_{ik}\tilde{W}_{jk} + \tilde{b}_{jk}\tilde{W}_{ik}),$$

where all the coefficients are obtained inserting the values in Table 1 in the blending function (14) described below. In the above equation $\tilde{k}$ is the turbulent kinetic energy and ϵ is the specific dissipation. The tensors appearing in equation (3) are the anisotropy tensor and II its second invariant,

$$\tilde{b}_{ij} = \frac{\tilde{R}_{ij}}{2\tilde{k}} - \frac{\delta_{ij}}{3} \quad , \qquad II = \tilde{b}_{ij}\tilde{b}_{ij} \quad , \tag{4}$$

$\tilde{S}$ the strain rate tensor, $\tilde{W}$ the rotation tensor

$$\tilde{S}_{ij} = \frac{1}{2}\left(\frac{\partial \tilde{U}_i}{\partial x_j} + \frac{\partial \tilde{U}_j}{\partial x_i}\right), \quad \tilde{W}_{ij} = \frac{1}{2}\left(\frac{\partial \tilde{U}_i}{\partial x_j} - \frac{\partial \tilde{U}_j}{\partial x_i}\right) \tag{5}$$

and $\tilde{S}_{ij}^*$ the traceless strain rate tensor. Finally, the specific dissipation is computed from the length scal.

$$\epsilon = C_\mu \tilde{k}\omega \quad , \tag{6}$$

where C_μ=0.09.

Table 1: Coefficients of SSG and LRR model for the re-distribution term [1]

	C_1	C_1^*	C_2	C_3	C_3^*	C_4	C_5
SSG	3.4	1.8	4.2	0.8	1.3	1.25	0.4
LRR	3.6	0	0	0.8	0	2.0	1.11

The isotropic destruction term reads:

$$\bar{\rho}\epsilon_{ij} = \frac{2}{3}C_\mu\bar{\rho}\tilde{k}\omega\delta_{ij} \quad . \tag{7}$$

For what concerns the diffusion term the generalized gradient diffusion model is chosen:

$$\bar{\rho}D_{ij} = \frac{\partial}{\partial x_k}\left[\left(\bar{\mu}\delta_{kl} + D^{(GGD)}\frac{\tilde{\rho}}{\omega}\tilde{R}_{kl}\right)\frac{\partial \tilde{R}_{ij}}{\partial x_l}\right] . \tag{8}$$

The value of the constant $D^{(GGD)}$ is computed by the equation:

$$D^{(GGD)} = F\sigma^* + (1 - F)\frac{C_s}{C_\mu} \quad . \tag{9}$$

F is the blending equation in (14), σ^*= 0.5 and C_s=0.22.
Finally the term $\bar{\rho}M_{ij}$, which represents a measure of the effects of compressibility through variations in density, is neglected. The Menter ω-equation for RSM reads as follows:

$$\frac{\partial}{\partial t}(\bar{\rho}\omega) + \frac{\partial}{\partial x_k}(\bar{\rho}\tilde{U}_k\omega) = \bar{\rho}P^\omega - \bar{\rho}D^\omega + \frac{\partial}{\partial x_k}\left[\left(\bar{\mu} + \sigma_\omega\frac{\bar{\rho}\tilde{k}}{\omega}\right)\frac{\partial \omega}{\partial x_k}\right] + \bar{\rho}C_D \tag{10}$$

with the production term

$$\bar{\rho}P^\omega = -\alpha_\omega\frac{\omega}{\tilde{k}}\tilde{R}_{ik}\frac{\partial \tilde{U}_i}{\partial x_k} \quad , \tag{11}$$

the destruction term

$$\bar{\rho}D^\omega = \beta_\omega\bar{\rho}\omega^2 \tag{12}$$

and the cross-diffusion term

$$\bar{\rho}C_D = \sigma_d \frac{\bar{\rho}}{\omega} \max\left(\frac{\partial \tilde{k}}{\partial x_k} \frac{\partial \omega}{\partial x_k} ; 0 \right) \quad . \tag{13}$$

The coefficients of the ω-equation, listed in table (2) as well as those of the Reynolds stresses are blended using the following function:

$$\phi = F\phi^{LRR} + (1 - F)\phi^{SSG} \quad . \tag{14}$$

Table 2: Coefficients for ω-equation [1]

	α_ω	β_ω	σ_ω	σ_d
SSG	0.44	0.0828	0.856	$2\sigma_\omega^{SSG}$
LRR	0.5556	0.075	0.5	0

The blending function of Menter is defined as:

$$F = \tanh(\zeta^4) \quad , \quad \zeta = \min\left[\max\left(\frac{\sqrt{\tilde{k}}}{C_\mu \omega d}; \frac{500\bar{\mu}}{\bar{\rho}\omega d^2} \right); \frac{4\sigma_\omega^{(SSG)}\bar{\rho}\tilde{k}}{\bar{\rho}C_D^{(SSG)} d^2} \right]. \tag{15}$$

During the average process required by the RANS approach, some additional terms appear into the averaged Navier-Stokes equations representing the contribution of turbulence to the mean flow. The modeling of the Reynolds stress tensor has been largely discussed above. The turbulent heat flux is modeled as in eddy viscosity models using a Fourier type model:

$$q_k^{(t)} = -\lambda_t \frac{\partial \tilde{T}}{\partial x_k} \quad , \quad \text{with} \quad \lambda_t = \frac{C_p \mu_t}{Pr_t} , \tag{16}$$

where $\tilde{T}$ is the mean temperature and λ_t the eddy heat conductivity. The eddy viscosity model can be obtained through the other turbulence variables using the equation:

$$\mu_t = \frac{\bar{\rho}\tilde{k}}{\omega} . \tag{17}$$

The turbulent Prandtl number is set constant and equal to $Pr_t = 0.9$.

The last term is the diffusion of the turbulent kinetic energy associated with the turbulent transport and diffusion terms and modeled as half the trace of the Reynolds stresses diffusion term:

$$\overline{\rho}D^{(k)} \approx \frac{\overline{\rho}D_{kk}}{2} \quad . \tag{18}$$

4. Boundary Conditions

At solid walls a non-slip condition is imposed for the velocity components and for the Reynolds stresses. For the ω-equation, the Menter approach is chosen:

$$\omega_w = C_m \frac{(\mu_l)_w}{0.075 \cdot d^2} \quad , \tag{19}$$

where the wall temperature used for computing the laminar viscosity is considered constant, d is the wall distance of the first cell center and C_m is a constant and is usually set to 10. Free stream conditions for the turbulent variables are:

$$\tilde{k}_\infty = \frac{3}{2}(\mathrm{I} \cdot \mathrm{M}_\infty \cdot \mathrm{c}_\infty)^2 \;, \quad \tilde{\mathrm{R}}_{\mathrm{ij}\infty} = \frac{2}{3}\tilde{k}_\infty \;, \quad \tilde{\omega}_\infty = \frac{\rho_\infty \cdot \tilde{k}_\infty \cdot \mathrm{Re}_\infty}{\mu_{\mathrm{t}\infty}} \;, \tag{20}$$

where M_∞ is the freestream Mach number and I the turbulence intensity. Outgoing Riemann invariants are determined by quantities being extrapolated from the interior domain, while incoming Riemann invariants are set by free stream conditions.

5. Results

Two test cases have been studied so far. A two-dimensional hypersonic double wedge and a three-dimensional hypersonic inlet based on the double wedge configuration.

5.1. 2D double wedge

At the inflow the following free stream conditions have been imposed: M=8.3, Re=3.76X10^6 and T=102 K. For what concerns the turbulent variables a turbulent intensity of 0.5% is chosen. The wall temperature is fixed at 300 K.

5.1.1. Grid Convergence study for two-dimensionale double wedge

The configuration consists of a blunt leading edge with a radius of 0.5mm, a first ramp with an angle of 9 degrees and a second ramp with an angle of 20.5 degrees. The grid is refined in the nose region and near the kink to better capture the flow structures. A grid convergence study has been performed using a coarse mesh (Figure 2) with 40000 points, a medium mesh with 80000 points and a fine mesh with 120000 points. The solution has been computed using a laminar/turbulent approach. The first ramp is computed laminar by forcing the turbulent source term to be zero. The second ramp is computed as fully turbulent. This approach allows us to simulate the transition process in the separated shear layer above the second ramp. The results
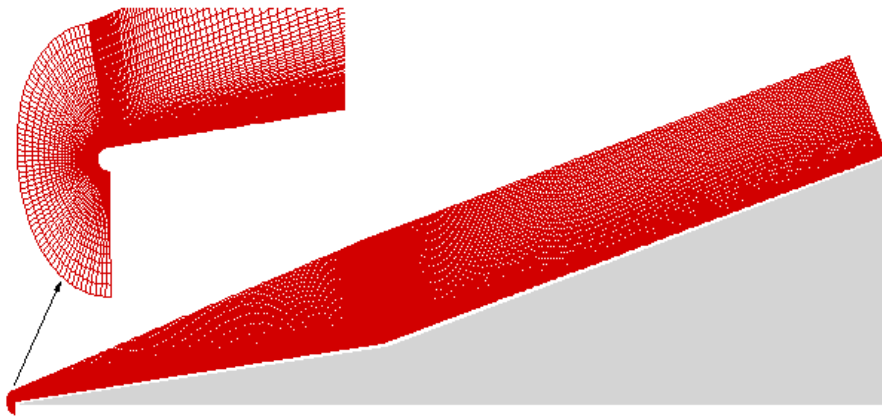

Figure 2: Grid for the medium mesh

for the pressure coefficient and the Stanton number are compared in Figure 5.1.1. The resolution of the coarse grid does not allow a reliable description of the flow field at the wall. For what concerns the medium and fine grid only small differences can be notice for pressure coefficient

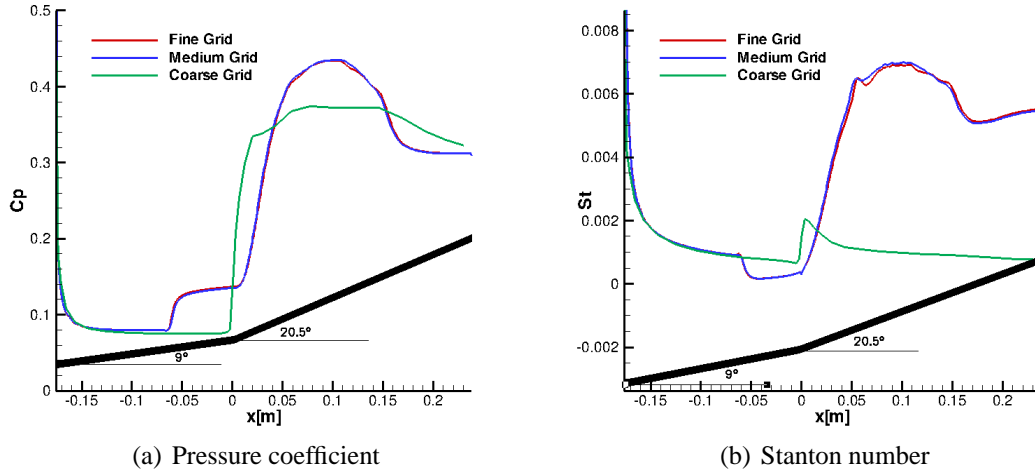(a) Pressure coefficient

(b) Stanton number

Figure 3: Distributions along a double wedge configuration with blunt leading edge using different grid refinements.

and for Stanton number. For these reasons the grid with 80000 points has been used for further investigations. The results obtained with the chosen grid has been used for a comparison with experimental [11] and numerical results using a transition model based on the SST turbulence model also available in QUADFLOW [12]. In Figure 4 the behavior of the pressure coefficient
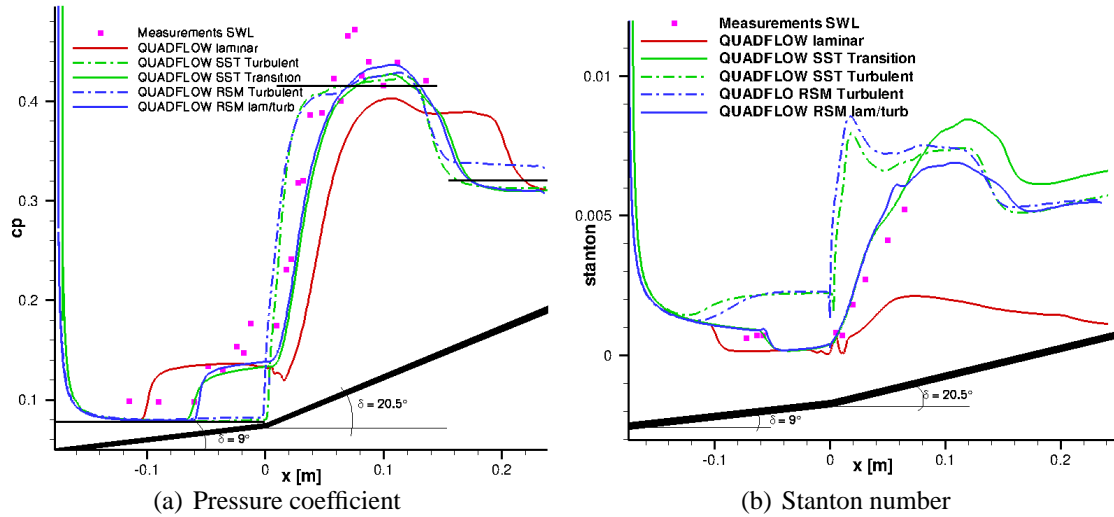

(a) Pressure coefficient

(b) Stanton number

Figure 4: Distributions along a double wedge configuration with blunt leading edge.

along the wall is shown. The black horizontal lines represent the pressure values obtained from the theory of oblique shock. We notice that the pressure value along the first ramp is the same for all the computational results but it is lower than the experimental one. This probably indicates that the inflow conditions for the experimental test were different from the nominal ones later used for the simulations. A higher pressure value is also observed along the second ramp where the pressure-peak measured in the shock tunnel is not reached by the simulations. A complete laminar simulation overpredict the size of the separation, specified by the first pressure rise due

to the separation shock followed by a region of constant pressure over the separation bubble and terminated by the second steep pressure rise due to the reattachment shock. The subsequent pressure decrease is due to the expansion fan originating from the intersection of the separation and the reattachment shock (see Figure 1). The fully turbulent profile obtained with the RSM is in good agreement with the SST model, however the fully turbulent flow does not separate. A laminar/turbulent simulation, with the Reynolds Stress Model, has been performed here since the fully turbulent solution does not capture the separation of the boundary layer and shows values significantly different from the experimental results. From the results, it can be noticed that the boundary layer separates along the first ramp and the size of the separation is smaller than that shown by the laminar solution. After the kink the pressure increases, as predicted by the theory, with a slope bigger than in the laminar case and reaches the theoretical value. Along the second ramp a further change in the pressure coefficient can be observed due to the merging of the two shock waves. The use of a combined laminar/turbulent simulations allows a good agreement with the transitional model and an improved agreement with the experimental results. The Stanton coefficient is also shown in Figure 4. The Stanton number distribution was the main reason for considering transitional flow in the first place since the experimental data clearly show a laminar behavior on the first ramp, however, turbulent levels in the area of peak heating on the second ramp were measured. For what concerns the RSM with laminar first ramp, the Stanton number decreases correctly along the first ramp following the laminar result and a further abrupt decrease occurs when the separation takes place. Also in this case, the size of the separation is smaller than that observed in a laminar simulation and is in agreement with the experiments. After the kink the Stanton number recovers but the values it takes are always higher than those from the wind tunnel experiment.

5.1.2. Adaptive Results

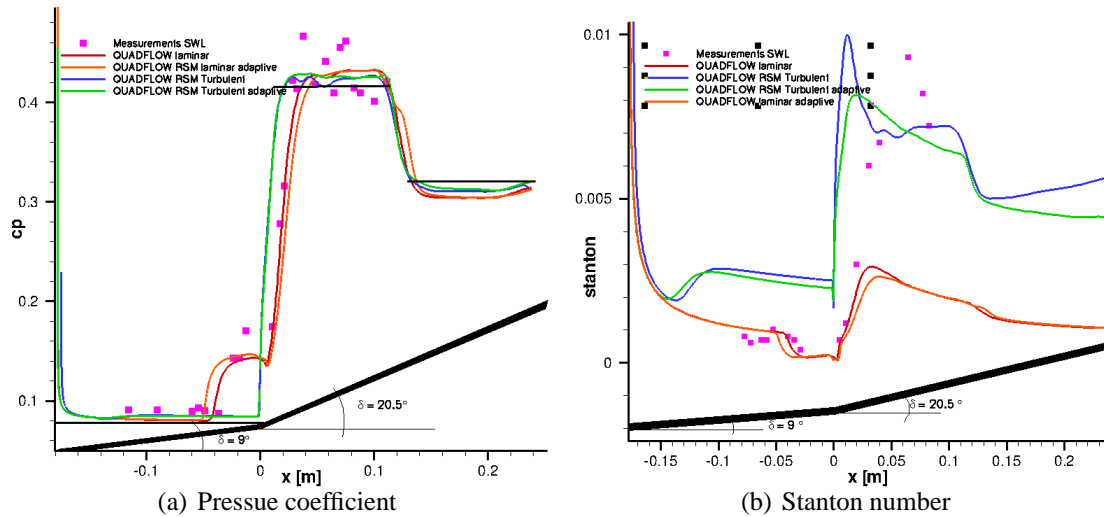(a) Pressue coefficient   (b) Stanton number

Figure 5: Distributions along a double wedge with sharp leading edge using adaptation.

The test case presented in the above paragraph with sharp leading edge has been used for testing the adaptive module. Adaptation is performed considering the five main variable and the first turbulent variable. Seven level of adaptation are performed (i.e. $l = 7$) in order to reach a correct grid resolution in the boundary layer. Figure 5 presents the pressure coefficient

and the Stanton number along the double wedge. For what concerns the pressure coefficient the numerical results with and without adaptation are in good agreement. The separation size is larger in the laminar adaptive simulation for unknown reasons. Considering the Stanton number, the numerical results show a similar behavior along the first ramp but significant differences can be seen along the second ramp. In the fully turbulent solution a considerable disagreement can be seen in the peak value and in the general behavior of the curve. A better agreement is shown in the laminar simulation. The reason for these discrepancies are still under investigation.

5.2. 3D inlet

A three-dimensional inlet with side walls, cowl and isolator has been considered as in Figure 6. As inflow conditions a free stream Mach number of 7, a Reynolds number of 4 Millions, a temperature of 46 K and a turbulence intensity of 0.2% have been chosen. The wall temperature is fixed at 300 K. A grid of approximately 6 Millions cells has been used for the simulation and the results are compared with experimental results [13]. A fully turbulent simulation has been performed at the moment as preliminary study. A laminar/turbulent simulation has been started but numerical instabilities, to be further investigated, did not allow the solution to converge. Further on adaptive simulation on 3D test cases will be run. Figure 7 shows the Mach number
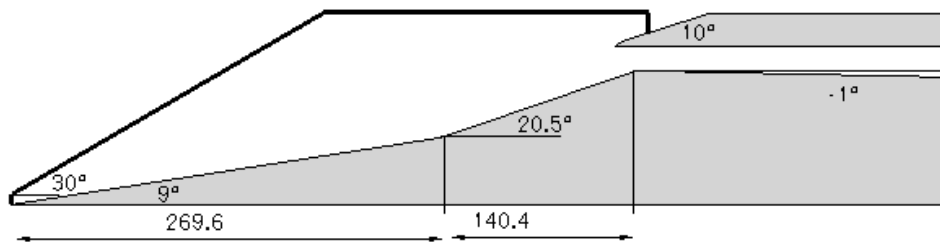

Figure 6: Sketch of the intake.

distribution resulting from a fully turbulent Reynolds stress model simulation using the model described here. A first ramp shock can be identified as a difference in Mach number along the vertical planes. Because of the turbulent boundary layer prescribed in the simulation, no separation can be seen in the kink region and a second shock originates at the beginning of the second ramp. This shock hits then the bow shock generated by the cowl lip in a point above the cowl. A separation bubble is created where the cowl shock impinges on the lower isolator wall and its size is approximately half of the isolator height. Because of the sidewalls, further shocks are generated and these help increasing the compression of the incoming flow. Vortices are generated along the side walls and the ramps whose sizes increase as they move downstream and influence the separation bubble in the isolator which is larger near the wall. The pressure coefficient along the wall at both ramp and cowl side has been investigated and compared with the experimental results. In Figure 8, we see the behavior, along the ramp. The use of a fully turbulent simulation has a strong influence on the shocks positions and on the peak pressure value achieved. It seems that the shock train along the isolator is anticipated. This hypothesis is confirmed from the pressure coefficient along the cowl side. Also in this case the shock position is different between numerical and experimental result and in the simulation the shock reflection is anticipated. Figure 9 show the Stanton distribution along the wall in
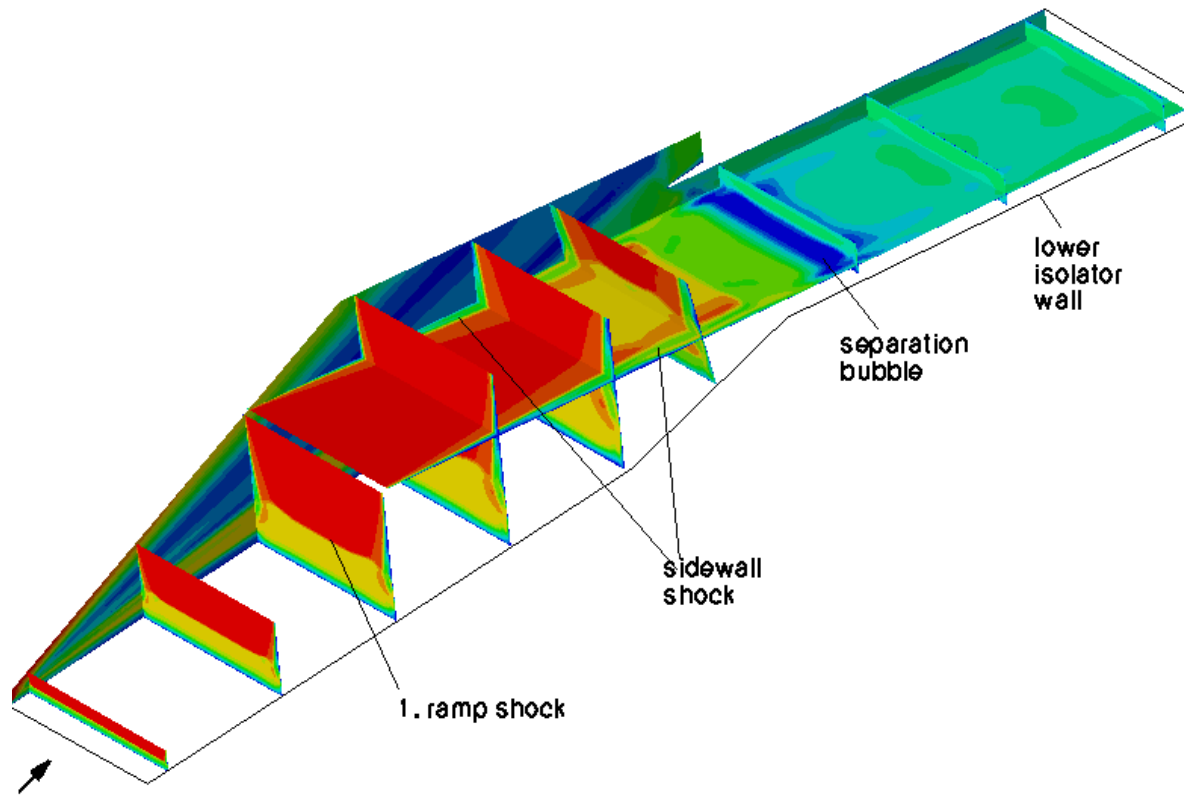
Figure 7: Mach number distribution along different planes.

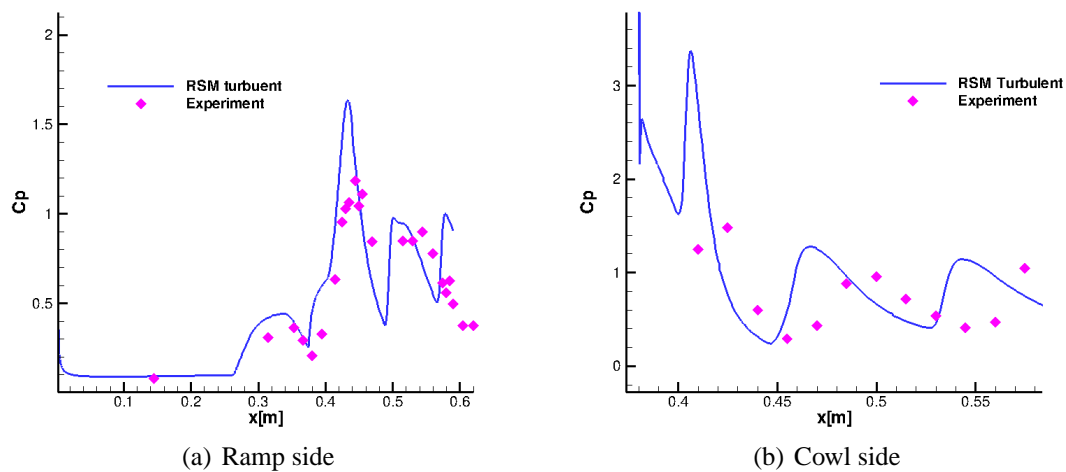(a) Ramp side   (b) Cowl side

Figure 8: Pressure coefficient distributions.

the kink region, the experimental results are obtained using infrared thermography. Once again it can be seen that the fully laminar solution is not able to predict the correct behavior of the heat fluxes. A sudden increase in the Stanton number can be seen just after the kink while in the experimental results the increase takes place in a smoother way. The two curves reach approximately the same peak value and then the coefficient decreases. A peak can be observed for the numerical simulation and this is due to some numerical instabilities caused by the strong

separation due to the impinging shock. Finally, in Figure 10 we present the value of Mach
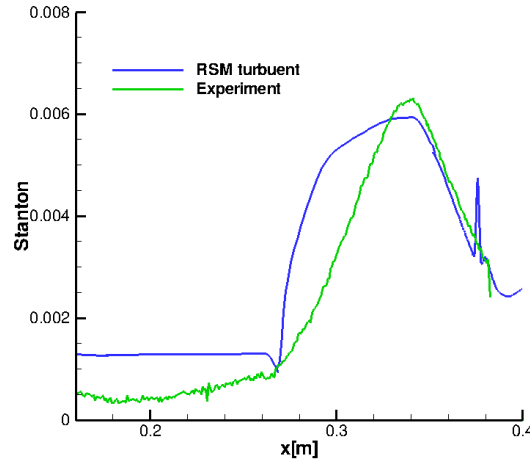

Figure 9: Stanton number distribution in the kink region at symmetry plane.

number and pitot pressure coefficient at the isolator exit symmetry plane. The value obtained for the Mach number show a general agreement with the experimental results. For what concerns the pitot pressure there is a great discrepancy concerning the third pressure probe from above. This is due to the fact that in this simulation the reflected shock does not 'hit' the measurement point and no peak pressure can be detected.
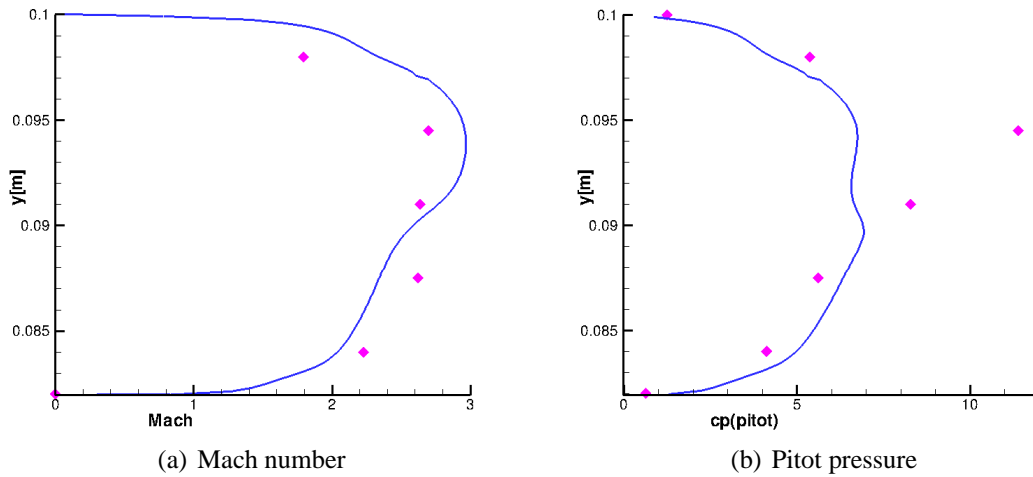

(a) Mach number   (b) Pitot pressure

Figure 10: Distributions at isolator exit symmetry plane.

6. Conclusion

The differential Reynolds stress model has been successfully implemented in the in-house code QUADFLOW. Results on a two-dimensional test case show a good agreement with other numerical and experimental results. The application of the adaptive module to hypersonic configuration is still under study and discrepancies with non-adaptive solution have to be further

investigated. Three-dimensional results show the need of a combined laminar-turbulent simulation to match the experimental results.

Acknowledgements

References

1. B. Eisfeld and O. Brodersen. Advanced Turbulence Modelling and Stress Analysis for the DLR-F5 Configuration. *AIAA Paper*, 2005-4727, 2005.

2. A. Bosco, B. Reinartz and S. Müller. Reynolds Stress Model implementation for hypersonic flow simulations. In *DGLR Kongress 2008*, 2008.

3. F. Bramkamp, Ph. Lamby and S. Müller. An adaptive multiscale finite volume solver for unsteady and steady state flow computations. In *J. of Computational Physics*, 197:460-490, 2004.

4. Y. Wada and M. S. Liou A Flux Splitting Scheme with High-Resolution and Robustness for discontinuities. In *AIAA Paper* , 94-0083, 1994.

5. B. Reinartz and J. Ballmann. Computation of Hypersonic Double Wedge Shock/Boundary Layer Interaction. In *26th International Symposium on Shock Waves*, 2007.

6. B.R. Launder, G.J. Reece and W. Rodi. Progress in the development of a Reynolds-stress turbulence closure. In *J. of Fluid Mechanics*, 68:537-566, 1975.

7. C.G. Speziale, S. Sarkar and T.B. Gatski. Modelling the pressure-strain correlation of turbulence: an invariant dynamical system approach. In *J. of Fluid Mechanics*, 227:254-272, 1991.

8. D.C. Wilcox Turbulence Modeling for CFD. *DCW Industries Inc*, 1993.

9. F.R. Menter and R.B. Langtry. A Correlation-Based Transition Model Using Local Variables Part 1- Model Formulation. In *Proceeding of ASME Turbo Expo*, 2004.

10. F.R. Menter. Two-Equation Eddy-Viscosity Turbulence Models for Engineering Applications. In *AIAA J*, 32:1598-1605, 1994.

11. T. Neuenhahn and H. Olivier. Influence of the wall temperature and the entropy layer effects on double wedge shock boundary layer interactions. In *AIAA Paper*, 2006-8136, 2006.

12. M. Krause and J. Ballmann. Application of a correlation-based intermittency transition model for hypersonic flows. In *DGLR Kongress 2008*, 2008.

13. J. Häberle and A. Gülhan Experimental Investigation of a Two-Dimensional and Three-Dimensional Inlet at Mach 7. In *J. of Propulsion and Power*, 24:1023:1034, 2008.